ACS central science

http://pubs.acs.org/journal/acscii

Research Article

Anomalous Interfacial Electron-Transfer Kinetics in Twisted Trilayer Graphene Caused by Layer-Specific Localization

Kaidi Zhang, Yun Yu, Stephen Carr, Mohammad Babar, Ziyan Zhu, Bryan Junsuh Kim, Catherine Groschner, Nikta Khaloo, Takashi Taniguchi, Kenji Watanabe, Venkatasubramanian Viswanathan, and D. Kwabena Bediako*

Cite This: *ACS Cent. Sci.* 2023, 9, 1119–1128

Read Online

ACCESS | Metrics & More | Article Recommendations | Supporting Information

ABSTRACT: Interfacial electron-transfer (ET) reactions underpin the interconversion of electrical and chemical energy. It is known that the electronic state of electrodes strongly influences ET rates because of differences in the electronic density of states (DOS) across metals, semimetals, and semiconductors. Here, by controlling interlayer twists in well-defined trilayer graphene moirés, we show that ET rates are strikingly dependent on electronic localization in each atomic layer and not the overall DOS. The large degree of tunability inherent to moiré electrodes leads to local ET kinetics that range over 3 orders of magnitude across different constructions of only three atomic layers, even exceeding rates at bulk metals. Our results demonstrate that beyond the ensemble DOS, electronic localization is critical in facilitating interfacial ET, with implications for understanding the origin of high interfacial reactivity typically exhibited by defects at electrode−electrolyte interfaces.

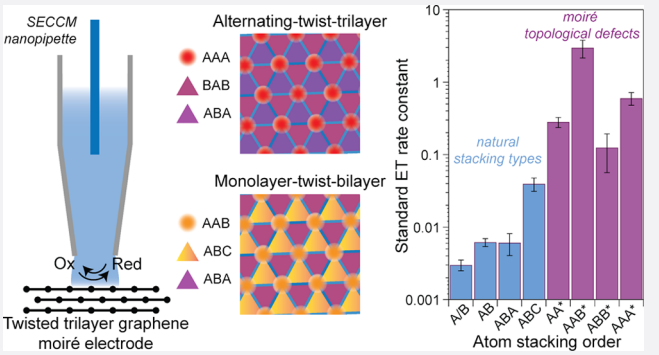

INTRODUCTION

Electron-transfer (ET) reactions at electrode−electrolyte interfaces are fundamental to electrochemical energy conversion.[1−3] The collective of microscopic theories and models for interfacial ET, inclucing the Marcus−Gerischer formalism,[4−9] the so-called Marcus−Hush−Chidsey (MHC) model,[10,11] and the density of states (DOS)−incorporated MHC (MHC−DOS) model,[12] highlight the importance of the electronic structure of an electrode on heterogeneous electrochemical rates. These frameworks motivate the discovery of new approaches to manipulate the band structure of electrodes as a means of controlling the performance limits of energy conversion and storage devices. Even though the electrode DOS was originally treated as invariant with energy/overpotential and delocalized, recent work has shown that the energy-dependence of the DOS can be an important factor in electrochemical reactions.[12] Furthermore, the effect of local DOS beyond the global electrode DOS has been identified as critical in understanding interfacial ET kinetics. On semiconductor or semimetallic electrodes, local electronic structure differences have been shown to affect ET kinetics,[13] and atomic defects at electrode surfaces provide a striking, albeit challenging to control, example of the pronounced effect of local structural/electronic modifications on interfacial reactivity. Atomic vacancies,[14] kinks, and step edges[15−17] are typically associated with massively enhanced interfacial reactivity compared to atomically pristine surfaces. The effect of these defects is typically explained in the context of providing increased DOS at energies that are desirable for charge transfer or the formation of a surface-bound catalytic intermediate (such as midgap states in a semiconducting material.[14,15]) However, the dangling bonds at such sites would invariably introduce a strong spatial localization of these large electronic DOS. For this reason, beyond the augmented DOS magnitude, we might consider that localization may play a key role in facilitating interfacial ET to the necessarily localized electronic states on the solution-phase molecule/complex/ion. However, a systematic experimental examination of the effects of electronic localization on heterogeneous interfacial charge transfer has been intractable owing to the considerable synthetic challenge of constructing pristine electrode materials that would allow a deterministic modulation of this property separate from the overall DOS.

Azimuthal misalignment of atomically thin layers produces moiré superlattices and alters the electronic band structure, in

Received: March 17, 2023
Published: May 15, 2023

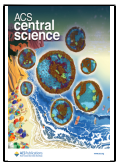

a manner that is systematically dependent on the interlayer twist angle.[18,19] The formation of flat electronic bands, particularly at a series of "magic" moiré angles, leads to a diversity of correlated electron physics.[20−23] Notably, these flat bands imply a large DOS that is highly localized in real space.[24] Small-angle twisted bilayer graphene (TBG) exhibits recently discovered angle-dependent electrochemical behavior,[25] where outer-sphere ET kinetics can be tuned nearly 10-fold simply by varying the moiré twist angle, θ_m, between 0 and 2°.

The stacking order of graphene in multilayers strongly alters the resulting electronic properties of the system.[21,26−34] As shown in SI Figure 1, whereas Bernal (ABA-stacked) trilayer graphene displays dispersive bands, rhombohedral (ABC) graphene possesses a nondispersive, or "flat", electronic band close to the Fermi level, which is responsible for the emergence of correlated electron phenomena at low temperatures.[35,36]

More pronounced flat bands are produced in twisted trilayer graphene (TTG) structures. A rotationally misaligned (by a moiré "twist" angle θ_m) monolayer and a Bernal stacked bilayer form a "monolayer-twist-bilayer" (M-*t*-B) heterostructure (Figure 1A).[37,38] Systematically alternating the angle between

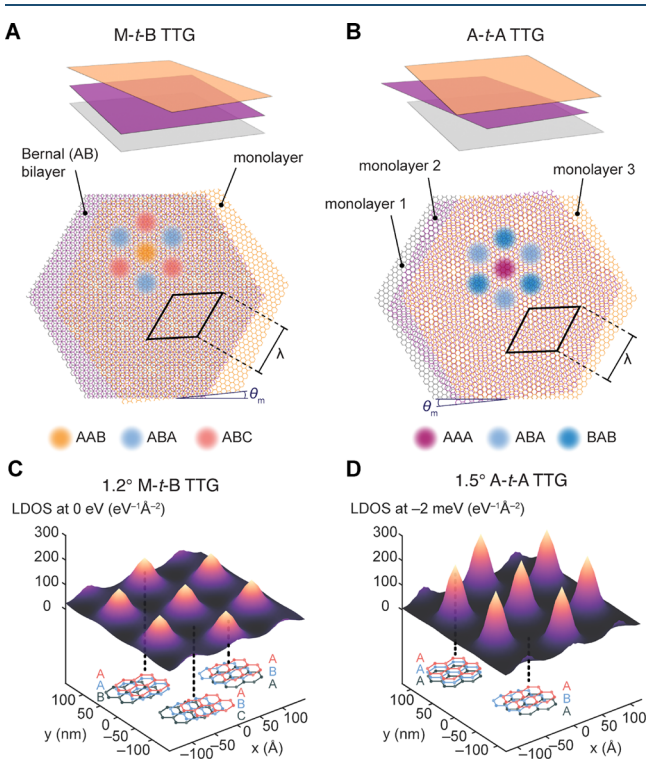

Figure 1. Polytypes of twisted trilayer graphene. (A, B) Illustrations of two twisted trilayer graphene polytypes, with moiré wavelength λ. The black parallelogram outlines the moiré unit cell in each case. (C, D) Computed local DOS (see Materials and Methods) for 1.2° M-*t*-B (C) and 1.5° A-*t*-A (D).

adjacent graphene layers such that the top layer is perfectly aligned with the bottom layer results in an "A-*t*-A" heterostructure (Figure 1B)[21,27,34] that possesses extremely flat bands at a magic angle of around 1.5° (SI Figure 1). These flattened electronic bands, which manifest as a large DOS that is localized on AAB and AAA sites in M-*t*-B and A-*t*-A TTG, respectively (Figure 1C,D), now introduce distinctive possibilities for systematically probing the dependence of interfacial ET on electronic structure generally and, in particular, the effects of electronic localization. For example, even within the TTG family, larger DOSs are found in A-*t*-A as compared to M-*t*-B near their respective magic angles (Figure 1C,D), properties that naively might be expected to correlate with interfacial ET rates, based on the MHC model.

RESULTS AND DISCUSSION

Scanning electrochemical cell microscopy (SECCM)[17] measurements were carried out on nontwisted (ABA, ABC) and twisted trilayer graphene samples that were fabricated into devices (see Materials and Methods).[25] As shown in Figure 2A, naturally occurring ABA and ABC trilayers were mechanically exfoliated from bulk graphite and identified using optical microscopy together with confocal Raman spectroscopy (see Materials and Methods and Supporting Information).[39,40] M-*t*-B and A-*t*-A TTG samples were prepared by the "cut-and-stack" approach (see Materials and Methods), resulting in samples possessing uniform θ_m around the magic angles of about 1.34° for an M-*t*-B device and 1.53° for an A-*t*-A device. Piezoelectric force microscopy (PFM) and scanning tunneling microscopy (STM) were used to evaluate the twist angle distribution and uniformity across the moiré samples (Figure 2B).[41] Using SECCM, cyclic voltammograms (CVs) were measured with 2.0 mM $Ru(NH_3)_6^{3+}$—an ideal and well-established redox couple for interrogating outer-sphere ET kinetics[16,25]—and 0.10 M KCl as the supporting electrolyte. In Figure 2C, a representative set of CVs collected from these different trilayer samples is shown. We find that the ABA domain of the flake shown in Figure 2A exhibited the most sluggish rates of $Ru(NH_3)_6^{3+}$ electro-reduction, as evinced by a half-wave potential ($E_{1/2}$) of −0.32 V, which is cathodically shifted substantially from the equilibrium potential, E^0, of −0.25 V for $Ru(NH_3)_6^{3+/2+}$ (all potentials are reported relative to the Ag/AgCl quasi-counter/reference electrode). However, the $E_{1/2}$ measured from the CV acquired in region II (ABC domain) of the same flake was −0.27 V, pointing to considerably more facile electroreduction kinetics on the rhombohedral trilayer as compared to the Bernal trilayer. For both TTG samples, reversible CVs with $E_{1/2} \approx -0.25$ V were obtained, indicative of highly facile electrokinetics and heterogeneous electrochemical rate constants that exceed those of both ABA and ABC graphene considerably. These observations motivated the measurement of the variation of interfacial ET rates with θ_m.

To quantitatively assess differences in interfacial kinetics associated with disparate electronic structures, we compared experimental CVs to those simulated with different standard rate constants, k^0, calculated with the Butler−Volmer model (see Materials and Methods and the Supporting Information). Here, it is critical to account for the relatively small and potential-dependent quantum capacitance, C_q (see Materials and Methods and Supporting Information)[16,25] in these low-dimensional electrodes, which for a given applied potential, V_{app}, produces a dynamic electron or hole doping of the few-layer graphene by an energy of eV_q (where e is the elementary charge and V_q is the chemical potential relative to the charge neutrality potential). The remainder, V_{dl}, persists as a drop across the electric double layer (so that $V_{app} = V_q + V_{dl}$). $C_q(V_q)$ was calculated for all trilayer systems (ABA and ABC as well as M-*t*-B and A-*t*-A at various θ_m values) (Figure 3A) using the respective computed band structures and DOS profiles (see Materials and Methods). The corresponding plots of V_{dl}/V_{app} as a function of V_{app} are shown in Figure 3B. Taken

https://doi.org/10.1021/acscentsci.3c00326
ACS Cent. Sci. 2023, 9, 1119−1128

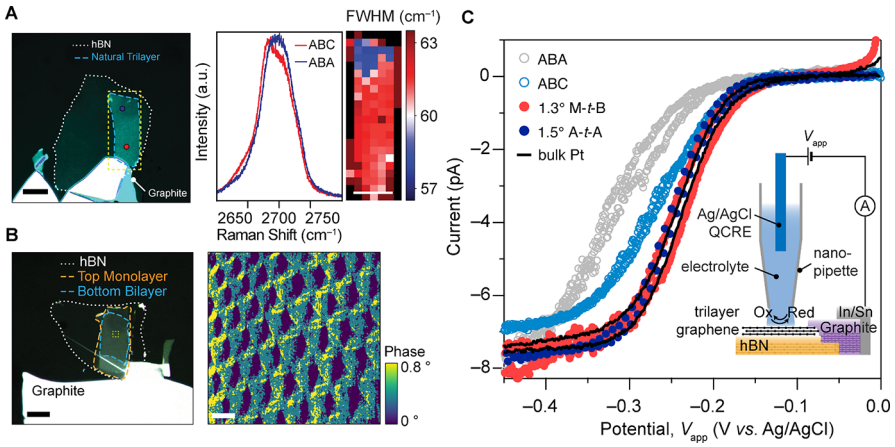

Figure 2. Fabrication and electrochemistry of twisted trilayer graphene. (A) Left: Optical micrograph of a device fabricated from an exfoliated trilayer graphene flake on hBN. Right: Confocal Raman spectra acquired in the sites in A marked with red (ABC domain) and blue (ABA domain) dots, along with the Raman map of the region indicated with a yellow box in A. Scale bars: 10 μm. (B) Left: Optical micrograph of an M-*t*-B device on hBN (Scale bar: 10 μm). Right: A lateral PFM phase image over the yellow boxed region in B reveals the moiré superlattice pattern. Scale bar: 50 nm. (C) Representative steady-state voltammograms of 2 mM $Ru(NH_3)_6^{3+}$ in 0.1 M KCl solution obtained at ABA and ABC trilayer graphene, along with 1.3° M-*t*-B and 1.5° A-*t*-A, compared to that obtained at an ∼40-nm-thick platinum film. Scan rate, 100 mV s^{-1}. The inset illustrates the SECCM technique.

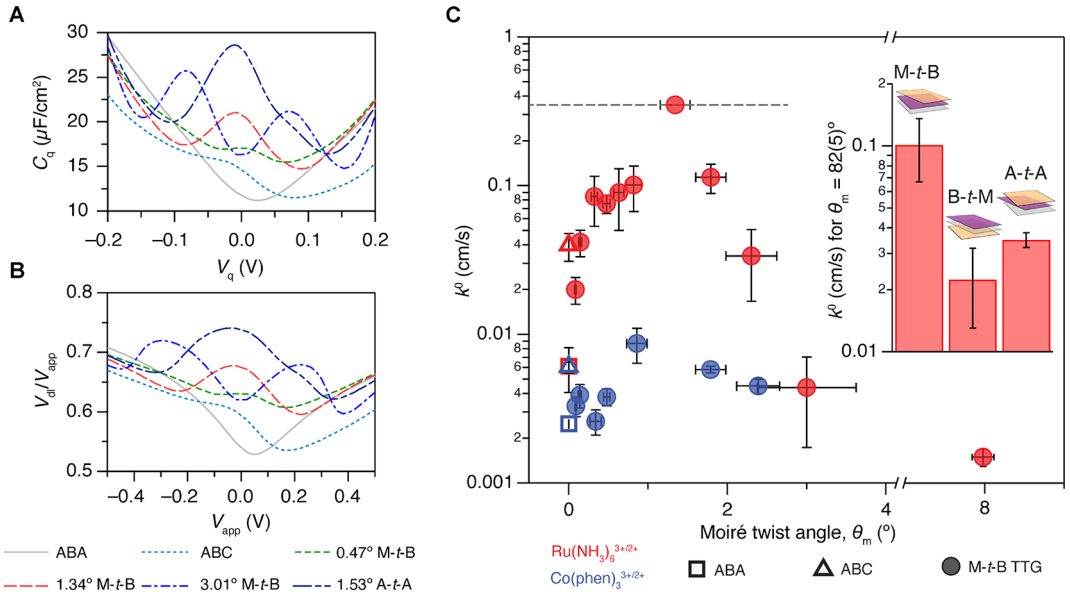

Figure 3. Angle-dependent quantum capacitance and interfacial ET. (A) Calculated C_q as a function of the chemical potential (V_q) for ABA, ABC, and TTG using the respective computed band structures and DOS profiles (see Materials and Methods). (B) Calculated fraction of applied potential on the double layer (V_{dl}/V_{app}) as a function of the applied potential (V_{app}) for ABA, ABC, and TTG. V_q and V_{app} are relative to the charge neutrality potential. Taken together, these data reveal that flat electronic bands result in a more significant fraction of V_{app} partitioning into V_{dl} near the charge neutrality potential. (C) Dependence of the ET rate constant, k^0, on the trilayer graphene stacking type (ABA, ABC) and θ_m for M-*t*-B TTG. Each marker denotes the mean of measurements made on samples within a standard deviation of the mean twist angle. The horizontal and vertical error bars represent the standard deviations of θ_m and the standard error of k^0. The inset shows comparison of k^0 values for M-*t*-B, B-*t*-M, and A-*t*-A TTG at θ_m = 0.82 ± 0.05°.

together, these data reveal that flat electronic bands result in a more significant fraction of V_{app} partitioning into V_{dl} near the charge neutrality potential. Notably, as shown in Figure 3A, changes in θ_m tune $C_q(V_q)$ and magic-angle (∼1.5°) A-*t*-A displays a higher C_q than magic-angle (1.2−1.3°) M-*t*-B, consistent with its overall greater DOS (Figure 1D).

After determining V_{dl} in this manner, we extracted k^0 values by identifying the simulated CV that was in closest agreement with the experiment[25] (see Materials and Methods and Supporting Information). The θ_m dependence of k^0 was measured by preparing M-*t*-B TTG devices with varying θ_m between 0.08 and 8.0° (see Materials and Methods) and acquiring CVs of $Ru(NH_3)_6^{3+}$ electroreduction by SECCM for each sample. Figure 3C shows the strong, nonmonotonic variation in k^0 over 2 orders of magnitude from ABA and ABC graphene to θ_m = 8° M-*t*-B. For samples with 1° ≤ θ_m ≤ 2°, ET appears to be reversible within our accessible scan rates, so we cannot extract any kinetic information beyond noting that within this range of θ_m, k^0 ≥ 0.35 cm/s. The quenched dependence of θ_m on k^0 (blue markers in Figure 3C) in analogous electrochemical measurements of the trisphenanthroline cobalt(III/II) redox couple, $Co(phen)_3^{3+/2+}$ (see

https://doi.org/10.1021/acscentsci.3c00326
ACS Cent. Sci. 2023, 9, 1119−1128

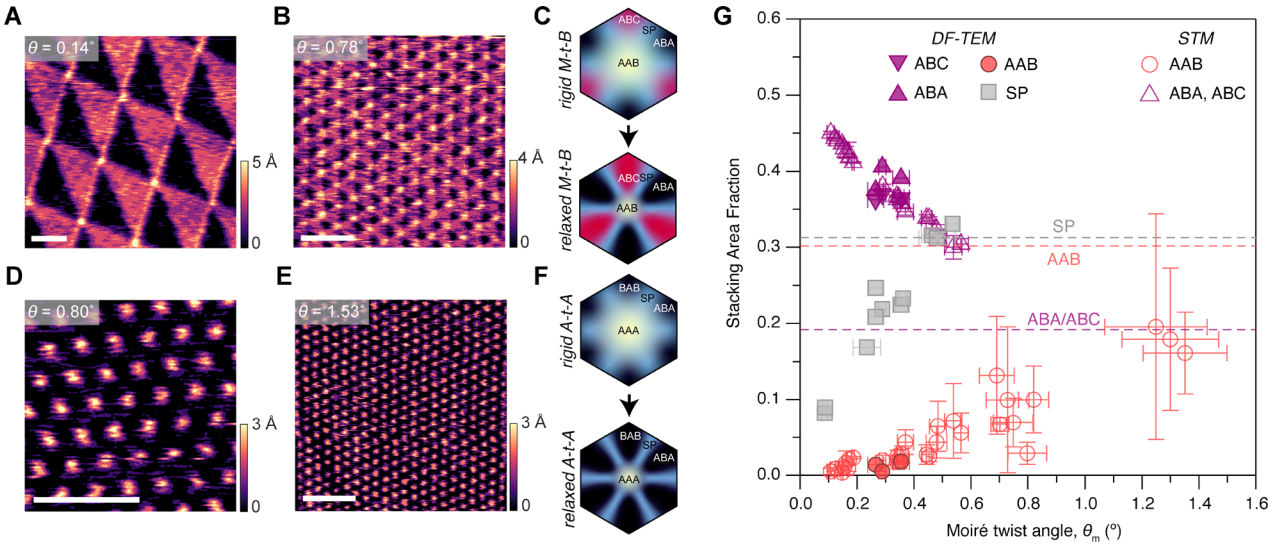

Figure 4. Lattice relaxation and stacking area fractions in TTG. (A, B, D, E) Constant-current STM images representative M-*t*-B (A, B) and A-*t*-A (D, E) samples. Scale bars: 50 nm. (C, D) Qualitative illustrations of different stacking domains in rigid and relaxed M-*t*-B (C) and A-*t*-A (F) moiré unit cells. (G) Extracted area fraction of different stacking domains in M-*t*-B TTG. The horizontal and vertical error bars represent the standard deviations of θ_m and the standard error of the area fraction, respectively.

Materials and Methods and Supporting Information) provides compelling evidence that it is the moiré flat bands that drive the observed angle-dependent electrokinetic modulation in TTG, as in TBG.[25]

An unexpected observation of the factors controlling interfacial ET is made by comparing the electrochemical responses of TTG polytypes. A-*t*-A TTG, on the basis of its massive DOS (SI Figure 1 and Figure 1D) and giant C_q—which exceeds that of M-*t*-B (Figure 3A)—should be expected to yield the highest ET rates. However, while an effect of θ_m on k^0 is also observed in A-*t*-A samples (see Supporting Information Table 1), this variant of TTG displays consistently lower k^0 than M-*t*-B at similar θ_m values (Figure 3C, inset). Furthermore, B-*t*-M heterostructures, which consist of a Bernal bilayer placed with a twist atop a monolayer (i.e., flipped versions of M-*t*-B), display markedly lower k^0 values than the corresponding M-*t*-B electrodes, notwithstanding an ostensibly identical overall electronic structure. These striking observations point clearly to effects governing the interfacial ET kinetics beyond simply the ensemble DOS.

To fully understand these θ_m dependencies as well as the disparities among the interfacial electron transfer kinetics of M-*t*-B, B-*t*-M, and A-*t*-A, we used STM (room temperature, constant current) to evaluate the role of lattice relaxation in controlling the area fraction of stacking domains in M-*t*-B and A-*t*-A TTG. In Figure 4A, a representative STM map of small-angle (θ_m = 0.14°) M-*t*-B shows a clear contrast among the various stacking domains. Regions with higher local DOS appear brighter than those with lower DOS since a larger tip–sample distance is required to maintain a constant current.[38] ABC domains, therefore, appear brighter than ABA domains owing to the native flat band of the ABC stacking type (SI Figure 1). These ABA and ABC domains (black and red regions, respectively) form alternating triangular patterns while the AAB region forms small circles of diameter ∼11 nm, which appear with the brightest contrast owing to the localization of the moiré flat band and associated large DOS on these AAB sites as shown in Figure 1C and SI Figure S2 (this is analogous to the localization of moiré flat bands on AA sites in TBG[24]).

For θ_m = 0.78° (Figure 4B), while the triangular ABA/ABC patterns have shrunk in size compared to those in Figure 4A, the diameters of AAB regions remained largely unchanged. For A-*t*-A, AAA domains are visible as bright spots (Figure 4D,E), consistent with the localization of the large DOS on these regions (Figure 1D and SI Figure 2),[42] with degenerate ABA and BAB regions requiring smaller tip–sample distances (dark regions) to sustain a constant STM current because of a lower local DOS.

The measured area distribution of stacking domains in TTG, therefore, differs significantly from those of rigid moiré structures. Both structures relax as depicted schematically in Figure 4C,F minimizing (maximizing) high (low) energy domains in a manner that is conceptually analogous to that reported for TBG.[24,43,44] To support these experiments, we also performed finite element method (FEM) simulations to model relaxation in TTG (see SI Figure 3 and Supporting Information), finding results that lie in good agreement with our STM and dark-field transmission electron microscopy (SI Figure 4) data. Importantly, these structural measurements and calculations permit a quantitative determination of the area fractions in TTG after reconstruction as a function of θ_m as plotted in Figure 4G (see also SI Figure 5 and Supporting Information Table 2).

These area fraction distributions after structural relaxation explain the origin of the kinetic modulation observed in Figure 3C at $\theta_m < 2°$ as being driven by θ_m-dependent area fractions of the "topological defect"[45,46] AAB and AAA sites. Our relaxation simulations (SI Figure 2) also show that at $\theta_m \leq 0.3°$ the relaxation of these moiré superlattices reestablishes nearly commensurate ABA, BAB, and/or ABC domains with local DOS that should not deviate substantially from those of freestanding ABA and ABC trilayers. This observation is in line with previous experimental[38,43,44,46] and theoretical studies[46,47] of lattice relaxation in bilayer analogues. Therefore, by considering k^0 variations at $\theta_m < 1°$ in Figure 3C (which are also within the range of kinetically resolvable k^0), we can extract the local rate constant associated with the AAB and AAA stacking domains through eqs 1 and 2 where β_i and κ_i^0

https://doi.org/10.1021/acscentsci.3c00326
ACS Cent. Sci. 2023, 9, 1119−1128

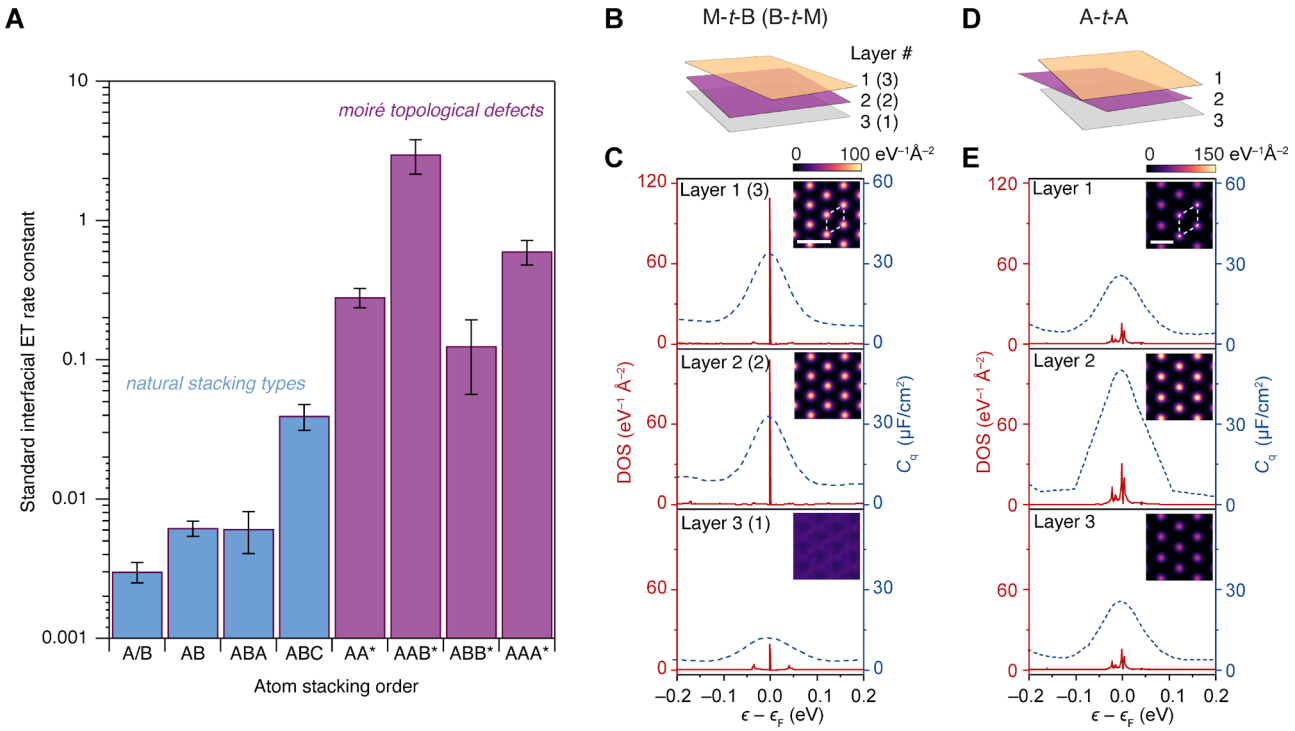

Figure 5. ET rates of few-layer graphene and layer-dependent DOS localization. (A) Local standard $Ru(NH_3)_6^{3+/2+}$ ET rate constants at few-layer graphene in different stacking configurations. "Artificial" moiré-derived stacking domains are labeled with an asterisk. Each bar is the mean local rate either measured (for natural stacking) or calculated (for aritifical stacking) for small twist angle samples. The error bars represent the standard errors for the rates. (B) Schematic of M-*t*-B/B-*t*-M graphene layers. (C) Layer-dependent DOS profile (see Materials and Methods and Supporting Information Text) for AAB stacking domains in M-*t*-B and B-*t*-M graphene at $\theta_m = 1.2°$. Insets show real space DOS maps of each layer at $\epsilon = -3$ meV. (D) Schematic of the A-*t*-A layers. (E) Layer-dependent DOS profile for AAA stacking domains in A-*t*-A graphene at $\theta_m = 1.2°$. The insets show real space DOS maps of each layer at $\epsilon = -1$ meV for $\theta_m = 1.2°$.

represent the area fraction and local standard heterogeneous ET rate constant, respectively, for stacking domain *i*.

$$k^0_{MtB} = \beta_{AAB}\kappa^0_{AAB} + \beta_{ABC}\kappa^0_{ABC} + \beta_{ABA}\kappa^0_{ABA} + \beta_{SP}\kappa^0_{SP} \quad (1)$$

$$k^0_{AtA} = \beta_{AAA}\kappa^0_{AAA} + \beta_{ABA}\kappa^0_{ABA} + \beta_{BAB}\kappa^0_{BAB} + \beta_{SP}\kappa^0_{SP} \quad (2)$$

As a result of the lattice relaxation effect discussed above, we can determine κ_{ABA} and κ_{ABC} from independent measurements of freestanding Bernal and rhombohedral trilayers (Figures 2C and 3C). In addition, we can assume that $\kappa^0_{SP} \approx \kappa^0_{ABA}$, which is justified on the basis of the STM images and calculated local DOS (see SI Figure 2). This analysis allows us to extract standard electron-transfer rate constants for the AAB (M-*t*-B), ABB (B-*t*-M), and AAA (A-*t*-A) topological defects.

Combined with previous electrochemical measurements at TBG surfaces,[25] we compare the ET kinetics of $Ru(NH_3)_6^{3+/2+}$ among a wide array of stacking configurations from monolayer to trilayer graphene in Figure 5A. For atomic stacking orders naturally found in bulk graphite, we observed a gradual enhancement as the number of layers increases from a monolayer to a Bernal trilayer. This can be explained by a modest increase in DOS close to the Fermi level as the number of layers increases.[16] ABC graphene displays a pronounced augmentation in k^0 from that of ABA graphene due to the intrinsic flat band of the rhombohedral system (SI Figure 1). Most notably, "artificial" high-energy stacking (AA, AAA, AAB, and ABB) topological defects created by moiré superlattices exhibit extraordinarily high k^0 values, with that of AAB exceeding 3 cm/s, which is greater than that measured on bulk platinum electrodes (0.85−1.2 cm/s),[48] notwithstanding consisting of only three atomic layers (see also Supporting Information Table 2).

Figure 5A also shows the unexpected result that AAA sites display lower ET rates than AAB notwithstanding the higher DOS and C_q of AAA than those of AAB (SI Figure 1 and Figure 3A). Strikingly, we also find that ABB sites yield slower ET kinetics than both AAB (despite identical overall DOS) and AA (despite higher overall DOS). Thus, while in-plane electronic localization and structural relaxation effects explain the dependence of k^0 on θ_m in TTG, the relative interfacial ET rates of AAB (M-*t*-B), ABB (B-*t*-M), and AAA (A-*t*-A) (Figure 3C inset and Figure 5A) appear not to correlate with DOS.

To explain these trends, Figure 5C−E shows layer-isolated local DOS(ϵ) and $C_q(\epsilon)$ profiles (Figure 5C,E) at the topological defects (AAB/ABB, AAA) along with calculated real-space DOS maps (insets in Figure 5C,E). Supporting Information Figure 6 contains layer-dependent DOS at other twist angles. These calculations show how the DOS enhancements at AAB sites are distinctly localized on the top two layers of M-*t*-B structures (i.e., the "AA" portions of AAB).[49] In contrast, the DOSs at AAA sites are most strongly localized on the middle layer of A-*t*-A. This three-dimensional electronic localization (within a thickness of only three atomic layers) arising from different symmetries of these topological defects unveils the fundamental basis for the unexpected trends in ET rate constants at AAB, ABB, and AAA (Figures 3C and 5A): though the electrodes are only three atomic layers thick, ET rate constants are correlated only with the electronic properties precisely at the electrode−electrolyte interface.

https://doi.org/10.1021/acscentsci.3c00326
ACS Cent. Sci. 2023, 9, 1119−1128

These observations strongly hint at the role of interfacial electronic coupling (between the localized states on the electrode and the electron donor/acceptor in solution), electric double-layer effects, and/or interfacial reorganization energy as even more crucial than the overall DOS alone. Indeed, theoretical calculations based on the MHC model that accounts only for the θ_m-dependent DOS but with a coupling strength, ν, and reorganization energy, λ, that are invariant with θ_m (see Supporting Information text and SI Figure 7) vastly underestimate the dependence of k^0 on θ_m. These MHC calculations also likewise predict identical interfacial ET rates for M-*t*-B and B-*t*-M, which is clearly at odds with the experiment. Our experimental results, therefore, now motivate future theoretical work to adapt these MHC models to consider how electronic localization, which is deterministically tuned here by varying θ_m or TTG structure, modifies ν[50] and/or λ[51] to bridge the gap between theory and experiment and extend our microscopic understanding of interfacial ET.

CONCLUSIONS

Controlling stacking geometries and twist angles in few-layer graphene, therefore, enables the manipulation of standard ET rate constants over 3 orders of magnitude. In particular, energetically unfavorable topological defects (AAA and AAB stacking domains), which are attainable only through the construction of a moiré superlattice, exhibit extraordinarily high standard rate constants. This electrochemical behavior arises from the moiré-derived flat bands that are localized in these topological defects. In addition to the effects of in-plane structural relaxation and electronic localization, the out-of-plane localization of the electron wave function on specific layers of twisted trilayer graphene results in measurable differences in ET rates at topological defects possessing different symmetries.

These results provide a powerful demonstration of the sensitivity of interfacial ET kinetics to the three-dimensional localization of electronic states at electrochemical surfaces and raise the question of whether traditional measurements of ET rates at macroscopic electrodes might severely underestimate the true local rate constant, which may be mediated by atomic defects that strongly localize electronic DOS at these interfaces. In turn, SECCM measurements are shown to be powerful tools for probing layer-dependent electronic localization in atomic heterostructure electrodes.

Future experimental and theoretical work is needed to shed more light on the microscopic origin of these electron-transfer modulations in the context of reorganization energy, electronic coupling, and even the electric double-layer structure. This work also heralds the use of moiré materials as a versatile and systematically tunable experimental platform for theoretical adaptations of the MHC framework applied to interfaces with localized electronic states, which are representative of defective surfaces that are ubiquitous to nearly all real electrochemical systems. In an applied context, twistronics is shown to be a powerful pathway for engineering pristine 2D material surfaces to execute charge-transfer processes with facile kinetics, holding implications for electrocatalysis[52,53] and other energy conversion device schemes that could benefit from ultrathin, flexible, and/or transparent electrodes that retain high electron-transfer kinetics.

MATERIALS AND METHODS

Chemicals. Natural Kish graphite crystals were purchased from Graphene Supermarket. Si/SiO_2 wafers (0.5 mm thick with 285 nm SiO_2 or 90 nm SiO_2) were purchased from NOVA Electronic Materials. Polydimethylsiloxane (PDMS) stamps were purchased from MTI Corporation. Sn/In alloy was purchased from Custom Thermoelectric. Poly(bisphenol A carbonate) (Mw 45 000), dichlorodimethylsilane (>99.5%), hexaammineruthenium(III) chloride (98%), cobalt(II) chloride hexahydrate (98%), 1,10-phenanthroline (>99%), calcium chloride (>93%), and potassium chloride (>99%) were purchased from Sigma-Aldrich and used as received. All aqueous electrolyte solutions were prepared with type I water (EMD Millipore, 18.2 MΩ cm resistivity). The 2 mM solutions of tris(1,10-phenanthroline)cobalt(II) were prepared by dissolving 1:3 molar ratios of solid cobalt(II) chloride and 1,10-phenanthroline in water. In both $Ru(NH_3)_6^{3+/2+}$ and $Co(phen)3^{3+}$ solutions, 0.1 M KCl was added as a supporting electrolyte.

Sample Fabrication. Graphite and hexagonal boron nitride (hBN) were exfoliated from the bulk crystals with Scotch tape. Exfoliated films were surveyed with an optical microscope (Laxco LMC-5000). Monolayer, bilayer, and trilayer graphene were identified with their characteristic optical contrasts of 7, 12, and 18%, respectively, in the green channel.[54] Trilayer graphene films were further confirmed by Raman spectroscopy (HORIBA LabRAM Evo) of the 2D peak (around 2600−2700 cm^{-1}).[39] The 2D peak was used to distinguish different stacking domains (ABC/ABA) as ABC trilayer graphene exhibits an enhanced shoulder at around 2640 cm^{-1} (see Supporting Information text). Trilayer graphene and twisted trilayer graphene samples were fabricated by the well-established "cut and stack" dry transfer method.[25] All transfers were carried out on a temperature-controlled heating stage (Instec), an optical microscope (Mitutoyo FS70), and a micromanipulator (MP-285, Sutter Instrument). For monolayer twist bilayer or bilayer twist monolayer samples, graphene flakes with both bilayer and monolayer parts were carefully selected. The monolayer section was severed from the bilayer with a scanning tunneling microscopy (STM) tip. For a-twist-a samples, a large piece of graphene (>50 μm by 20 μm) was cut evenly into three pieces. A thin piece of poly(bisphenol A carbonate) (PC) film (~3 × 3 mm^2) attached to a PDMS chunk (~7 × 7 mm^2) was used to pick up an hBN (~10−20 nm) from the SiO_2/Si substrate at 120 °C. This hBN was carefully aligned with the bottom layer of the graphene stack and lowered to pick up that piece. The stage was rotated (usually to a slightly larger angle than the desired twist), and the second piece of graphene was overlapped by the already picked-up graphene and thus delaminated from the substrate. For a-twist-a samples, a third piece of graphene was picked up after the stage was rotated back to the original orientation. A piece of graphite (~20 nm, >50 μm × 50 μm) was then picked up such that it was connected to the graphene. The PC film was carefully removed from the PDMS and placed onto a clean SiO_2/Si. In/Sn was painted onto the graphite via microsoldering[55] to a metallic plate which is attached beneath the SiO_2/Si.

Finite Element Simulation and Cyclic Voltammograms Fitting. All finite element simulations of electron transport were performed on a COMSOL Multiphysics v5.6 (COMSOL) to capture the effects of quantum capacitance

https://doi.org/10.1021/acscentsci.3c00326
ACS Cent. Sci. 2023, 9, 1119−1128

(see Supporting Information Text). The fitting of the CVs was achieved by statistical analysis of the experimental and simulated CVs (SI Figures 8 and 9).

Raman Mapping. Confocal Raman spectra were collected by recording from 2550−2800 cm^{-1} with a 532 nm laser at 3.2 mW. Raman maps were generated by collecting the spectrum across the trilayer films with a step size of 2 μm. The spectrum was fitted with single Lorentzian functions. The full-width at half maxima of the fitted functions were used to differentiate ABA and ABC trilayers (see Supporting Information text).

PFM Measurements. PFMs were performed on an AIST-NT OmegaScope Reflection. Ti/Ir-coated silicon probes from the Nanosensor with a force constant of 2.8 N m^{-1} and a resonance frequency of 75 kHz were used. A 2 V AC bias with resonance frequencies at 820 kHz was used, and the force was set to 25 nN.

STM Measurements. STM measurements were conducted using a Park NX10 STM module (Park Systems) at room temperature and atmospheric pressure. Pt−Ir tips were prepared by electrochemical etching of 0.25 mm Pt−Ir wires (Nanosurf) in 1.5 M $CaCl_2$ solutions.[56] The scanned images were taken with a 0.2 V tip−sample bias and a 100 pA current set point. More STM images of various samples can be found in SI Figure 10. Twist angles of various samples were determined using Delaunay triangulation on the Gaussian centers.[24,25]

Electron Microscopy Measurements. The transmission electron microscopy images of the nanopipettes (SI Figure 11) were obtained with a JEOL 1200EX transmission electron microscope operated at 100 keV. The top ∼1 mm portion of the pipette was attached to the grid (PELCO Hole Grids) such that the pipette tip was positioned in the center hole, and the rest of the pipette was broken off. Selected-area electron diffraction patterns were collected on an FEI Tecnai T20 S-TWIN transmission electron microscope with a LaB_6 filament operated at 200 kV. Selected area electron diffraction was used to resolve the twist angles for samples with twist angles larger than 3° (SI Figure 12). To obtain the diffraction patterns, the fabricated TLG/hBN samples were transferred onto a holey silicon nitride membrane after electrochemical measurements. Dark-field images shown in SI Figure 4 of TLG/hBN samples were measured at the National Center for Electron Microscopy facility in the Molecular Foundry at Lawrence Berkeley National Laboratory. Low-magnification DF-TEM images were acquired using a Gatan UltraScan camera on a Thermo Fisher Scientific Titan-class microscope operated at 60 kV.

Calculation of Band Structure and DOS. The DOS for trilayer graphene structures was calculated as a function of θ_m using the ab initio perturbation continuum model developed previously.[57] The low-energy electronic structure is based on a momentum expansion about the valley K point of the supercell Brillouin zone, allowing a smooth dependence of bands on the twist angle. It has been shown that the perturbation continuum model exactly reproduces the results of the more expensive ab initio tight-binding model, and both are in good agreement with full density functional theory (DFT) calculations.[57−60] The energy range of integration for the DOS was fixed at ±0.5 eV around the charge neutrality point (CNP). For evaluation of the LDOS, the normalized moiré supercell was divided into a 90 × 90 grid in real space and sampled over 36 k points in the Brillouin zone. We kept the sublattice symmetry intact and assumed no extra screening of the interlayer coupling constants.

Quantum Capacitance Calculation. Quantum capacitance (C_q) describes the variation of electrical charges with respect to the chemical potential (V_q). Theoretical C_q values with respect to V_q were calculated based on the following equation[61]

$$C_q = e^2 \int_{-\infty}^{+\infty} D(\epsilon) F_T(\epsilon - eV_q) d\epsilon \tag{3}$$

$$F_T(\epsilon) = (4k_B T)^{-1} \mathrm{sech}^2(\epsilon / 2k_B T) \tag{4}$$

where $D(\epsilon)$ is the density of states, which we center at the CNP, $F_T(\epsilon)$ is the thermal broadening function, and k_B is Boltzmann's constant. We assumed T = 300 K for our experimental conditions. The total electric double-layer capacitance is governed by the compact layer capacitance. Hence, we used a constant C_{dl} = 10 μF cm^{-2} to simplify the calculation.[62] We solved the self-consistent equations relating V_{app}, V_q, V_{dl}, C_q, and C_{dl} using Simpson integration and nonlinear least squares

$$V_{app} = V_{dl} + V_q \tag{5}$$

$$\frac{V_{dl}}{V_q} = \frac{C_q}{C_{dl}} \tag{6}$$

to obtain C_q vs V_q and V_{dl}/V_{app} vs V_{app} as shown in Figure 3.

SECCM Measurements. The SECCM nanopipettes were fabricated from single-channel quartz capillaries (inner and outer diameters of 0.7 mm and 1.0 mm from Sutter Instrument) in a laser nanopipet puller (Sutter Instrument model 2000). The program was set to heat 700, filament 4, velocity 20, delay 127, and pull 140 to generate pipettes of diameters around 200 nm, as later confirmed with bright-field TEM[25] (see SI Figure 11). The outer surfaces of the pipettes were silanized by dipping them into dichlorodimethylsilane for less than 1 s when nitrogen was flowed through the inside of the pipettes. They were then filled with either $Ru(NH_3)_6^{3+}$ or $Co(phen)_3^{3+}$ solutions through a microsyringe. The pipettes were gently tapped, and a gentle string of nitrogen was used to eliminate the bubbles. The pipettes were then inserted with a Ag/AgCl wire as a quasi-counter reference electrode (QCRE). The pipettes carefully approached (0.2 μm/s) the locations of interest while a −0.5 V (0.5 V for $Co(phen)_3^{3+}$) bias was applied. The meniscus achieved contact when a current of larger than 2 pA (or smaller than −2 pA) was observed. The pipette was allowed to stabilize for 30 s. Cyclic voltammograms (CVs) were then conducted by sweeping the potential at 100 mV s^{-1} between −0.6 and 0 V (0 to 0.8 V for $Co(phen)_3^{3+/2+}$) for five cycles. Multiple CVs were collected for each sample, and for small twist samples ($\theta \leq 0.15°$) with moiré wavelengths of more than 80 nm, only CVs recorded with nanopipettes of more than 200 nm in diameter were included to ensure that they surveyed multiple stacking domains. To survey electrochemical activities across a large sample, the pipette was retracted by 1 μm after CVs were measured and horizontally moved to a new location for a new approach.

■ ASSOCIATED CONTENT

Supporting Information

The Supporting Information is available free of charge at https://pubs.acs.org/doi/10.1021/acscentsci.3c00326.

Raman maps of ABA and ABC graphene, calculations of the areal fraction from STM and dark-field images, finite

https://doi.org/10.1021/acscentsci.3c00326
ACS Cent. Sci. 2023, 9, 1119−1128

element simulation of cyclic voltammagrams, Marcus−Hush−Chidsey calculations, area fraction determinations based on rigid and relaxed moiré, calculations of relaxation and the local twist angle of TTL, Supplementary Figures 1−19, and Supplementary Tables 1−3 (PDF)

AUTHOR INFORMATION

Corresponding Author

D. Kwabena Bediako − *Department of Chemistry, University of California, Berkeley, California 94720, United States; Chemical Sciences Division, Lawrence Berkeley National Laboratory, Berkeley, California 94720, United States;* orcid.org/0000-0003-0064-9814; Email: bediako@berkeley.edu

Authors

Kaidi Zhang − *Department of Chemistry, University of California, Berkeley, California 94720, United States*

Yun Yu − *Department of Chemistry, University of California, Berkeley, California 94720, United States;* Present Address: Current affiliation: Department of Chemistry and Biochemistry, George Mason University, Fairfax, VA 22030, United States

Stephen Carr − *Brown Theoretical Physics Center, Brown University, Providence, Rhode Island 02912, United States*

Mohammad Babar − *Department of Mechanical Engineering, Carnegie Mellon University, Pittsburgh, Pennsylvania 15213, United States;* orcid.org/0000-0001-6779-3859

Ziyan Zhu − *SLAC National Accelerator Laboratory, Menlo Park, California 94025, United States*

Bryan Junsuh Kim − *Department of Chemistry, University of California, Berkeley, California 94720, United States*

Catherine Groschner − *Department of Chemistry, University of California, Berkeley, California 94720, United States*

Nikta Khaloo − *Department of Chemistry, University of California, Berkeley, California 94720, United States*

Takashi Taniguchi − *International Center for Materials Nanoarchitectonics, National Institute for Materials Science, 305-0044 Tsukuba, Japan;* orcid.org/0000-0002-1467-3105

Kenji Watanabe − *Research Center for Functional Materials, National Institute for Materials Science, 305-0044 Tsukuba, Japan;* orcid.org/0000-0003-3701-8119

Venkatasubramanian Viswanathan − *Department of Mechanical Engineering, Carnegie Mellon University, Pittsburgh, Pennsylvania 15213, United States;* orcid.org/0000-0003-1060-5495

Complete contact information is available at: https://pubs.acs.org/10.1021/acscentsci.3c00326

Author Contributions

K.Z., Y.Y., and D.K.B. conceived the study. K.Z., B.J.K., C.G., and N.K. performed the experiments. K.Z. performed the COMSOL simulations. M.B., S.C., and V.V. carried out the theoretical calculations. K.Z. performed the quantum capacitance calculations. K.Z. and B.J.K. performed STM image analysis. T.T. and K.W. provided the hBN crystals. K.Z., Y.Y., and D.K.B. analyzed the data. K.Z. and D.K.B. wrote the manuscript with input from all coauthors.

Notes

The authors declare no competing financial interest.

ACKNOWLEDGMENTS

This material is based upon work supported by the U.S. Department of Energy, Office of Science, Office of Basic Energy Sciences, under award no. DE-SC0021049 (experimental studies by K.Z., Y.Y., B.J.K., N.K., and D.K.B.) and the Office of Naval Research under award no. N00014-180-S-F009 (computational work by M.B. and V.V.). S.C. acknowledges support from the National Science Foundation under grant no. OIA-1921199. C.G. was supported by a grant from the W. M. Keck Foundation (award no. 993922). Experimental work at the Molecular Foundry, LBNL was supported by the Office of Science, Office of Basic Energy Sciences, the U.S. Department of Energy under contract no. DE-AC02-05CH11231. Confocal Raman spectroscopy was supported by a Defense University Research Instrumentation Program grant through the Office of Naval Research under award no. N00014-20-1-2599 (D.K.B.). Other instrumentation used in this work was supported by grants from the Canadian Institute for Advanced Research (CIFAR−Azrieli Global Scholar, award no. GS21-011), the Gordon and Betty Moore Foundation EPiQS Initiative (award no. 10637), and the 3M Foundation through the 3M Non-Tenured Faculty Award (no. 67507585). K.W. and T.T. acknowledge support from JSPS KAKENHI (grant numbers 19H05790, 20H00354, and 21H05233). We thank Isaac M. Craig for the helpful discussion regarding STM analysis.

REFERENCES

(1) Seh, Z. W.; Kibsgaard, J.; Dickens, C. F.; Chorkendorff, I.; Nørskov, J. K.; Jaramillo, T. F. Combining theory and experiment in electrocatalysis: Insights into materials design. *Science* **2017**, *355*, eaad4998.

(2) Nørskov, J. K.; Bligaard, T.; Rossmeisl, J.; Christensen, C. H. Towards the computational design of solid catalysts. *Nat. Chem.* **2009**, *1*, 37−46.

(3) Hwang, J.; Rao, R. R.; Giordano, L.; Katayama, Y.; Yu, Y.; Shao-Horn, Y. Perovskites in catalysis and electrocatalysis. *Science* **2017**, *358*, 751−756.

(4) Schmickler, W.; Santos, E. *Interfacial Electrochemistry*; Springer Science & Business Media: 2010.

(5) Kuznetsov, A. *Charge Transfer in Physics, Chemistry and Biology: Physical Mechanisms of Elementary Processes and an Introduction to the Theory*; Gordon & Breach: 1995.

(6) Bard, A. J.; Faulkner, L. R.; White, H. S. *Electrochemical Methods: Fundamentals and Applications*; John Wiley & Sons: 2022.

(7) Santos, E.; Schmickler, W. Models of electron transfer at different electrode materials. *Chem. Rev.* **2022**, *122*, 10581−10598.

(8) Gerischer, H. Uber den Ablauf von Redoxreaktionen an Metallen und an Halbleitern. *Z. Phys. Chem. NF* **1960**, *26*, 223−247.

(9) Gerischer, H. Electron-transfer kinetics of redox reactions at the semiconductor/electrolyte contact. A new approach. *J. Phys. Chem.* **1991**, *95*, 1356−1359.

(10) Henstridge, M. C.; Laborda, E.; Rees, N. V.; Compton, R. G. Marcus-Hush-Chidsey theory of electron transfer applied to voltammetry: A review. *Electrochim. Acta* **2012**, *84*, 12−20.

(11) Zeng, Y.; Smith, R. B.; Bai, P.; Bazant, M. Z. Simple formula for Marcus-Hush-Chidsey kinetics. *J. Electroanal. Chem.* **2014**, *735*, 77−83.

(12) Kurchin, R.; Viswanathan, V. Marcus-Hush-Chidsey kinetics at electrode-electrolyte interfaces. *J. Chem. Phys.* **2020**, *153*, 134706.

(13) Patten, H. V.; Meadows, K. E.; Hutton, L. A.; Iacobini, J. G.; Battistel, D.; McKelvey, K.; Colburn, A. W.; Newton, M. E.; Macpherson, J. V.; Unwin, P. R. Electrochemical Mapping Reveals Direct Correlation between Heterogeneous Electron-Transfer Kinetics and Local Density of States in Diamond Electrodes. *Angew. Chem., Int. Ed.* **2012**, *51*, 7002−7006.

(14) Li, H.; Tsai, C.; Koh, A. L.; Cai, L.; Contryman, A. W.; Fragapane, A. H.; Zhao, J.; Han, H. S.; Manoharan, H. C.; Abild-Pedersen, F.; et al. Activating and optimizing MoS2 basal planes for hydrogen evolution through the formation of strained sulphur vacancies. *Nat. Mater.* **2016**, *15*, 48−53.
(15) Jaramillo, T. F.; Jørgensen, K. P.; Bonde, J.; Nielsen, J. H.; Horch, S.; Chorkendorff, I. Identification of Active Edge Sites for Electrochemical H2 Evolution from MoS2 Nanocatalysts. *Science* **2007**, *317*, 100−102.
(16) Güell, A. G.; Cuharuc, A. S.; Kim, Y.-R.; Zhang, G.; Tan, S.-y.; Ebejer, N.; Unwin, P. R. Redox-dependent spatially resolved electrochemistry at graphene and graphite step edges. *ACS Nano* **2015**, *9*, 3558−3571.
(17) Unwin, P. R.; Guell, A. G.; Zhang, G. Nanoscale electrochemistry of sp2 carbon materials: from graphite and graphene to carbon nanotubes. *Acc. Chem. Res.* **2016**, *49*, 2041−2048.
(18) Kim, K.; Yankowitz, M.; Fallahazad, B.; Kang, S.; Movva, H. C.; Huang, S.; Larentis, S.; Corbet, C. M.; Taniguchi, T.; Watanabe, K.; et al. van der Waals heterostructures with high accuracy rotational alignment. *Nano Lett.* **2016**, *16*, 1989−1995.
(19) Lau, C. N.; Bockrath, M. W.; Mak, K. F.; Zhang, F. Reproducibility in the fabrication and physics of moiré materials. *Nature* **2022**, *602*, 41−50.
(20) Cao, Y.; Fatemi, V.; Demir, A.; Fang, S.; Tomarken, S. L.; Luo, J. Y.; Sanchez-Yamagishi, J. D.; Watanabe, K.; Taniguchi, T.; Kaxiras, E.; et al. Correlated insulator behaviour at half-filling in magic-angle graphene superlattices. *Nature* **2018**, *556*, 80−84.
(21) Hao, Z.; Zimmerman, A.; Ledwith, P.; Khalaf, E.; Najafabadi, D. H.; Watanabe, K.; Taniguchi, T.; Vishwanath, A.; Kim, P. Electric field-tunable superconductivity in alternating-twist magic-angle trilayer graphene. *Science* **2021**, *371*, 1133−1138.
(22) Chen, G.; Jiang, L.; Wu, S.; Lyu, B.; Li, H.; Chittari, B. L.; Watanabe, K.; Taniguchi, T.; Shi, Z.; Jung, J.; et al. Evidence of a gate-tunable Mott insulator in a trilayer graphene moiré superlattice. *Nat. Phys.* **2019**, *15*, 237−241.
(23) Balents, L.; Dean, C. R.; Efetov, D. K.; Young, A. F. Superconductivity and strong correlations in moiré flat bands. *Nat. Phys.* **2020**, *16*, 725−733.
(24) Kerelsky, A.; McGilly, L. J.; Kennes, D. M.; Xian, L.; Yankowitz, M.; Chen, S.; Watanabe, K.; Taniguchi, T.; Hone, J.; Dean, C.; et al. Maximized electron interactions at the magic angle in twisted bilayer graphene. *Nature* **2019**, *572*, 95−100.
(25) Yu, Y.; Zhang, K.; Parks, H.; Babar, M.; Carr, S.; Craig, I. M.; Van Winkle, M.; Lyssenko, A.; Taniguchi, T.; Watanabe, K.; et al. Tunable angle-dependent electrochemistry at twisted bilayer graphene with moiré flat bands. *Nat. Chem.* **2022**, *14*, 267−273.
(26) Latychevskaia, T.; Son, S.-K.; Yang, Y.; Chancellor, D.; Brown, M.; Ozdemir, S.; Madan, I.; Berruto, G.; Carbone, F.; Mishchenko, A.; et al. Stacking transition in rhombohedral graphite. *Frontiers of Physics* **2019**, *14*, 13608.
(27) Fischer, A.; Goodwin, Z. A.; Mostofi, A. A.; Lischner, J.; Kennes, D. M.; Klebl, L. Unconventional superconductivity in magic-angle twisted trilayer graphene. *npj Quantum Materials* **2022**, *7*, 5.
(28) Latil, S.; Henrard, L. Charge carriers in few-layer graphene films. *Phys. Rev. Lett.* **2006**, *97*, 036803.
(29) Xu, R.; Yin, L.-J.; Qiao, J.-B.; Bai, K.-K.; Nie, J.-C.; He, L. Direct probing of the stacking order and electronic spectrum of rhombohedral trilayer graphene with scanning tunneling microscopy. *Phys. Rev. B* **2015**, *91*, 035410.
(30) Zhu, Z.; Carr, S.; Massatt, D.; Luskin, M.; Kaxiras, E. Twisted trilayer graphene: A precisely tunable platform for correlated electrons. *Phys. Rev. Lett.* **2020**, *125*, 116404.
(31) Li, H.; Utama, M. I. B.; Wang, S.; Zhao, W.; Zhao, S.; Xiao, X.; Jiang, Y.; Jiang, L.; Taniguchi, T.; Watanabe, K.; et al. Global control of stacking-order phase transition by doping and electric field in few-layer graphene. *Nano Lett.* **2020**, *20*, 3106−3112.
(32) Zhang, S.; Xu, Q.; Hou, Y.; Song, A.; Ma, Y.; Gao, L.; Zhu, M.; Ma, T.; Liu, L.; Feng, X.-Q.; et al. Domino-like stacking order switching in twisted monolayer-multilayer graphene. *Nat. Mater.* **2022**, *21*, 621−626.
(33) Park, Y.; Chittari, B. L.; Jung, J. Gate-tunable topological flat bands in twisted monolayer-bilayer graphene. *Phys. Rev. B* **2020**, *102*, 035411.
(34) Park, J. M.; Cao, Y.; Watanabe, K.; Taniguchi, T.; Jarillo-Herrero, P. Tunable strongly coupled superconductivity in magic-angle twisted trilayer graphene. *Nature* **2021**, *590*, 249−255.
(35) Zhou, H.; Xie, T.; Taniguchi, T.; Watanabe, K.; Young, A. F. Superconductivity in rhombohedral trilayer graphene. *Nature* **2021**, *598*, 434−438.
(36) Chen, G.; Sharpe, A. L.; Fox, E. J.; Zhang, Y.-H.; Wang, S.; Jiang, L.; Lyu, B.; Li, H.; Watanabe, K.; Taniguchi, T.; et al. Tunable correlated Chern insulator and ferromagnetism in a moiré superlattice. *Nature* **2020**, *579*, 56−61.
(37) Xu, S.; Al Ezzi, M. M.; Balakrishnan, N.; Garcia-Ruiz, A.; Tsim, B.; Mullan, C.; Barrier, J.; Xin, N.; Piot, B. A.; Taniguchi, T.; et al. Tunable van Hove singularities and correlated states in twisted monolayer-bilayer graphene. *Nat. Phys.* **2021**, *17*, 619−626.
(38) Li, S.-y.; Wang, Z.; Xue, Y.; Wang, Y.; Zhang, S.; Liu, J.; Zhu, Z.; Watanabe, K.; Taniguchi, T.; Gao, H.-j.; et al. Imaging topological and correlated insulating states in twisted monolayer-bilayer graphene. *Nat. Commun.* **2022**, *13*, 4225.
(39) Lui, C. H.; Li, Z.; Chen, Z.; Klimov, P. V.; Brus, L. E.; Heinz, T. F. Imaging stacking order in few-layer graphene. *Nano Lett.* **2011**, *11*, 164−169.
(40) Cong, C.; Yu, T.; Sato, K.; Shang, J.; Saito, R.; Dresselhaus, G. F.; Dresselhaus, M. S. Raman characterization of ABA-and ABC-stacked trilayer graphene. *ACS Nano* **2011**, *5*, 8760−8768.
(41) McGilly, L. J.; Kerelsky, A.; Finney, N. R.; Shapovalov, K.; Shih, E.-M.; Ghiotto, A.; Zeng, Y.; Moore, S. L.; Wu, W.; Bai, Y.; et al. Visualization of moiré superlattices. *Nat. Nanotechnol.* **2020**, *15*, 580−584.
(42) Turkel, S.; Swann, J.; Zhu, Z.; Christos, M.; Watanabe, K.; Taniguchi, T.; Sachdev, S.; Scheurer, M. S.; Kaxiras, E.; Dean, C. R.; et al. Orderly disorder in magic-angle twisted trilayer graphene. *Science* **2022**, *376*, 193−199.
(43) Yoo, H.; Engelke, R.; Carr, S.; Fang, S.; Zhang, K.; Cazeaux, P.; Sung, S. H.; Hovden, R.; Tsen, A. W.; Taniguchi, T.; et al. Atomic and electronic reconstruction at the van der Waals interface in twisted bilayer graphene. *Nat. Mater.* **2019**, *18*, 448−453.
(44) Kazmierczak, N. P.; Van Winkle, M.; Ophus, C.; Bustillo, K. C.; Carr, S.; Brown, H. G.; Ciston, J.; Taniguchi, T.; Watanabe, K.; Bediako, D. K. Strain fields in twisted bilayer graphene. *Nat. Mater.* **2021**, *20*, 956−963.
(45) McEuen, P. L. Strain solitons and topological defects in bilayer graphene. *Proc. National Acad. Sci.* **2013**, *110*, 11256−11260.
(46) Engelke, R.; Yoo, H.; Carr, S.; Xu, K.; Cazeaux, P.; Allen, R.; Valdivia, A. M.; Luskin, M.; Kaxiras, E.; Kim, M.; Han, J. H.; Kim, P. Non-Abelian topological defects and strain mapping in 2D moiré materials. *arXiv* 2022, DOI: 10.48550/arXiv.2207.05276.
(47) Carr, S.; Massatt, D.; Torrisi, S. B.; Cazeaux, P.; Luskin, M.; Kaxiras, E. Relaxation and domain formation in incommensurate two-dimensional heterostructures. *Phys. Rev. B* **2018**, *98*, 224102.
(48) Santos, E.; Iwasita, T.; Vielstich, W. On the use of the coulostatic method for the investigation of fast redox systems. *Electrochim. Acta* **1986**, *31*, 431−437.
(49) Tong, L.-H.; Tong, Q.; Yang, L.-Z.; Zhou, Y.-Y.; Wu, Q.; Tian, Y.; Zhang, L.; Zhang, L.; Qin, Z.; Yin, L.-J. Spectroscopic visualization of flat bands in magic-angle twisted monolayer-bilayer graphene: coexistence of localization and delocalization. *Phys. Rev. Lett.* **2022**, *128*, 126401.
(50) Pavlov, S. V.; Nazmutdinov, R. R.; Fedorov, M. V.; Kislenko, S. A. Role of graphene edges in the electron transfer kinetics: insight from theory and molecular modeling. *J. Phys. Chem. C* **2019**, *123*, 6627−6634.
(51) Limaye, A. M.; Ding, W.; Willard, A. P. Understanding attenuated solvent reorganization energies near electrode interfaces. *J. Chem. Phys.* **2020**, *152*, 114706.

https://doi.org/10.1021/acscentsci.3c00326
ACS Cent. Sci. 2023, 9, 1119−1128

(52) Yu, Y.; Van Winkle, M.; Bediako, D. K. Tuning interfacial chemistry with twistronics. *Trends Chem.* **2022**, *4*, 857−859.
(53) Zhang, Y.; Felser, C.; Fu, L. Moiré metal for catalysis. *arXiv* 2021, DOI: 10.48550/arXiv.2111.03058.
(54) Li, H.; Wu, J.; Huang, X.; Lu, G.; Yang, J.; Lu, X.; Xiong, Q.; Zhang, H. Rapid and reliable thickness identification of two-dimensional nanosheets using optical microscopy. *ACS Nano* **2013**, *7*, 10344−10353.
(55) Girit, Ç. Ö.; Zettl, A. Soldering to a single atomic layer. *Appl. Phys. Lett.* **2007**, *91*, 193512.
(56) Libioulle, L.; Houbion, Y.; Gilles, J.-M. Very sharp platinum tips for scanning tunneling microscopy. *Rev. Sci. Instrum.* **1995**, *66*, 97−100.
(57) Carr, S.; Fang, S.; Zhu, Z.; Kaxiras, E. Exact continuum model for low-energy electronic states of twisted bilayer graphene. *Phys. Rev. Research* **2019**, *1*, 013001.
(58) Carr, S.; Fang, S.; Kaxiras, E. Electronic-structure methods for twisted moiré layers. *Nat. Rev. Mater.* **2020**, *5*, 748−763.
(59) Fang, S.; Kaxiras, E. Electronic structure theory of weakly interacting bilayers. *Phys. Rev. B* **2016**, *93*, 235153.
(60) Lucignano, P.; Alfè, D.; Cataudella, V.; Ninno, D.; Cantele, G. Crucial role of atomic corrugation on the flat bands and energy gaps of twisted bilayer graphene at the magic angle θ 1. 08. *Phys. Rev. B* **2019**, *99*, 195419.
(61) Yang, G.; Zhang, H.; Fan, X.; Zheng, W. Density functional theory calculations for the quantum capacitance performance of graphene-based electrode material. *J. Phys. Chem. C* **2015**, *119*, 6464−6470.
(62) Xia, J.; Chen, F.; Li, J.; Tao, N. Measurement of the quantum capacitance of graphene. *Nat. Nanotechnol.* **2009**, *4*, 505−509.

https://doi.org/10.1021/acscentsci.3c00326
ACS Cent. Sci. 2023, 9, 1119−1128